Intratumoral TREX1 Induction Promotes Immune Evasion by Limiting Type I IFN

Eléonore Toufektchan[1], Alexandra Dananberg[1], Josefine Striepen[1], James H. Hickling[1], Abraham Shim[1], Yanyang Chen[1], Ashley Nichols[1], Mercedes A. Duran Paez[2], Lisa Mohr[1], Samuel F. Bakhoum[2,3], and John Maciejowski[1]

ABSTRACT

Chromosomal instability is a hallmark of human cancer that is associated with aggressive disease characteristics. Chromosome mis-segregations help fuel natural selection, but they risk provoking a cGAS-STING immune response through the accumulation of cytosolic DNA. The mechanisms of how tumors benefit from chromosomal instability while mitigating associated risks, such as enhanced immune surveillance, are poorly understood. Here, we identify cGAS-STING–dependent upregulation of the nuclease TREX1 as an adaptive, negative feedback mechanism that promotes immune evasion through digestion of cytosolic DNA. TREX1 loss diminishes tumor growth, prolongs survival of host animals, increases tumor immune infiltration, and potentiates response to immune checkpoint blockade selectively in tumors capable of mounting a type I IFN response downstream of STING. Together, these data demonstrate that TREX1 induction shields chromosomally unstable tumors from immune surveillance by dampening type I IFN production and suggest that TREX1 inhibitors might be used to selectively target tumors that have retained the inherent ability to mount an IFN response downstream of STING.

See related article by Lim et al., p. 663

Introduction

Chromosomal instability (CIN) is a hallmark of human cancer characterized by high rates of chromosome mis-segregation during mitosis (1). CIN is associated with poor prognosis, metastasis, and therapeutic resistance (2). In addition to fueling cancer genome evolution by promoting copy-number instability, chromosome segregation errors can result in the formation of micronuclei when a chromosome or chromosome fragment lags during anaphase and fails to join the main chromatin mass that will form the primary nucleus. Micronuclei assemble fragile envelopes that frequently rupture, exposing genomic double-stranded DNA (dsDNA) to the cytosol (3, 4). Micronuclear envelope rupture can elicit an immune response by enabling the cytosolic DNA sensor cGAS to productively engage genomic DNA (5–9). Binding to dsDNA in ruptured micronuclei stimulates cGAS catalytic activity, producing the second messenger 2′3′-cyclic GMP-AMP (cGAMP; refs. 10–13). cGAMP engagement with its downstream receptor STING results in TBK1-dependent activation of transcription factors including IRF3, ultimately resulting in the expression of type I IFNs and other immunomodulatory pathways (14–17).

The cGAS-STING cytosolic DNA-sensing pathway plays key roles in cancer immunosurveillance and immunotherapy (18–21). High levels of cytosolic DNA in chromosomally unstable cancer cells risk triggering an immune response through cGAS-STING activation. The adaptive mechanisms chromosomally unstable cancer cells use to evade immunity in the presence of high levels of cytosolic DNA are poorly understood. Immune escape can be accomplished by epigenetic silencing of cGAS or STING expression (22). Alternatively, some cancers co-opt the cGAS-STING pathway in a manner that silences type I IFN production downstream of STING in favor of noncanonical NFκB activation and associated metastatic spread (23, 24). Upregulation of ENPP1, an ectonucleotidase that negatively regulates cGAS by hydrolyzing extracellular cGAMP, enables some chromosomally unstable cancers to escape immune surveillance that can occur with tumor-to-host cGAMP transfer (25, 26). Additional mechanisms, including how cancer cells may utilize other cGAS-STING regulators, have not been well characterized.

TREX1 is an ER-associated, 3′→5′ DNA exonuclease that degrades cytosolic DNA to prevent chronic cGAS activation and consequent autoimmunity (27–31). Mutations in *TREX1* are associated with Aicardi-Goutières syndrome (AGS), an immune disease characterized by progressive neurologic dysfunction and high type I IFN levels (32, 33). *Trex1* knockout (KO) and TREX1 nuclease–deficient mice recapitulate hallmarks of this disease, including high IFN levels (27, 34–38). Importantly, the health of *Trex1*-deficient animals is restored by deletion of key proinflammatory proteins active in DNA sensing, such as *Cgas* and the type I IFN receptor component *Ifnar1*, implicating deficient cytosolic DNA degradation and chronic cGAS activation in the etiology of AGS (39, 40). We previously demonstrated that TREX1 inhibits cGAS activation at micronuclei (8), suggesting that TREX1-mediated degradation of micronuclear DNA may enable cancer cells to benefit from CIN while dampening excessive cGAS-STING activation and a downstream type I IFN response.

Here, we show that chronic cGAS-STING activation increases *Trex1* mRNA expression, TREX1 protein levels, and exonuclease activity in chromosomally unstable colorectal and breast cancer cells. Upregulation of TREX1 serves as an adaptive, negative feedback mechanism that dampens cGAS-STING activation, thereby limiting downstream type I IFN production. In accordance with these findings, intratumoral *Trex1* loss leads to diminished tumor growth and prolonged host survival in a mechanism that depends on intratumoral

[1]Molecular Biology Program, Sloan Kettering Institute, Memorial Sloan Kettering Cancer Center, New York, New York. [2]Human Oncology and Pathogenesis Program, Memorial Sloan Kettering Cancer Center, New York, New York. [3]Department of Radiation Oncology, Memorial Sloan Kettering Cancer Center, New York, New York.

Corresponding Author: John Maciejowski, Memorial Sloan Kettering Cancer Center, 1275 York Avenue, New York, NY 10065. E-mail: maciejoj@mskcc.org

Cancer Immunol Res 2024;12:673–86

doi: 10.1158/2326-6066.CIR-23-1093

cGAS-STING and host adaptive immunity. These effects depend on a capacity for type I IFN production in the tumor compartment downstream of STING and on an intact type I IFN receptor in the host compartment. Together, these results demonstrate that TREX1 upregulation is a key event that facilitates immune evasion of chromosomally unstable cancer cells by limiting cGAS-STING–dependent type I IFN signaling.

Materials and Methods

Cell lines and culture

CT26 (catalog no.CRL-2638), EO771.LMB (catalog no.CRL-3405), and 4T1 (catalog no. CRL-2539) cell lines were purchased from the ATCC. EO771.LMB cells were cultured in DMEM supplemented with 20 mmol/L HEPES and 10% FBS. CT26 and 4T1 cells were cultured in RPMI supplemented with 10% FBS. MCF10A cells were cultured in 1:1 mixture of F12:DMEM media supplemented with 5% horse serum (Thermo Fisher Scientific), 20 ng/mL human EGF (Millipore Sigma), 0.5 mg/mL hydrocortisone (Millipore Sigma), 100 ng/mL cholera toxin (Millipore Sigma), and 10 μg/mL recombinant human insulin (Millipore Sigma). All media was supplemented with 1% penicillin-streptomycin. Unless otherwise noted, all media and supplements were supplied by the Memorial Sloan Kettering Cancer Center (MSKCC) Media Preparation facility. Regular *Mycoplasma* testing was conducted using the LookOut Mycoplasma Elimination Kit (Millipore Sigma).

Cell lines were used for experiments within five passages or less of being thawed from frozen stocks. All cell lines were cultured in a humidified 5% CO_2 atmosphere at 37°C.

For all three cell lines, CT26, EO771.LMB, and 4T1, CRISPR-mediated KO of *Cgas* and *Sting1* were generated by nucleofecting the protein Cas9 (Integrated DNA Technologies, IDT) and single-guide RNA (sgRNA; IDT; *cGas*-sgRNA: GCGAGGGTCCAGGAAGGAAC; *Sting1*-sgRNA: CTACATAACAACATGCTCAG) using the Lipofectamine CRISPRMAX Cas9 Transfection Reagent (Thermo Fisher Scientific) according to the manufacturer's instructions, then isolating and expanding KO clones.

For EO771.LMB cells, CRISPR-mediated KOs of *Irf3* were generated by nucleofecting the protein Cas9 (IDT) and 3 sgRNAs (IDT; *Irf3*-sgRNA1: ATAAGCCGGACGTGTCAACC; *Irf3*-sgRNA2: ACGGGATCCTGAACCTCGTT; *Irf3*-sgRNA3: GGCCATCAAATAACTTCGGT), then isolating and expanding KO clones.

CRISPR-mediated KO of *Trex1* was generated by cotransfecting three different pU6-sg*Trex1*-Cas9-T2A-mCherry vectors assembled using the following oligonucleotides: Trex1-sgRNAF1: caccgAAGCTGAGCTGGAAGTACAG and Trex1-sgRNAR1: aaacCTGTACTTCCAGCTCAGCTT; Trex1-sgRNAF2: caccgCCTAGATGGTACCTTCTGTG and Trex1-sgRNAR2: aaacCACAGAAGGTACCATCTAGG; Trex1-sgRNAF3: aaacGGTCACCGTTGTGTGCCACA and Trex1-sgRNAR3: caccgTGTGGCACACAACGGTGACC; using Lipofectamine 3000 Transfection Reagent (Thermo Fisher Scientific) according to the manufacturer's instructions, then isolating and expanding the cells with KOs from single-cell colonies.

For each KO cell line, 5–12 single KO clones were selected and pooled to create a polyclonal population to mimic the heterogeneity of the parental cells.

MCF10A *cGAS* KO cells were generated as described previously (22).

Immunofluorescence microscopy

For immunofluorescence microscopy, CT26, EO771.LMB, and 4T1 cells were seeded on coverslips at 1.5×10^6 cells/mL 24 hours before fixation. Cells were carefully washed with PBS prior to fixation in 2% paraformaldehyde in PBS for 15 minutes. Coverslips were washed with PBS, incubated in permeabilization buffer (20 mmol/L Tris-HCl pH8, 50 mmol/L NaCl, 3 mmol/L $MgCl_2$, 300 mmol/L Sucrose, 0.5% Triton X-100) for 10 minutes and washed again with PBS. Coverslips were incubated in blocking buffer (1 mg/mL BSA, 3% goat serum, 0.1% Triton X-100, 1 mmol/L ethylenediamine tetraacetic acid (EDTA) in PBS) for 1 hour, and cGAS primary antibody (CST-31659, 1:500), diluted in blocking buffer, was added for 2 hours. After three washes with PBS-TX (PBS, 0.1%Triton X-100), coverslips were incubated with the secondary antibody (Goat anti-Rabbit IgG Alexa Fluor 488, Invitrogen, A11034, 1:1,000), diluted in blocking buffer, for 1 hour, then washed three times with PBS-TX. DNA was stained with Hoechst 33342 (Thermo Fisher Scientific, 1 μg/mL) for 15 minutes, before coverslips were washed two times with PBS. Coverslips were mounted in ProLong Gold Antifade Mountant (Life Technologies). Images were acquired on a Nikon Eclipse Ti2-E equipped with a CSU-W1 spinning disk with Borealis microadapter, Perfect Focus 4, motorized turret and encoded stage, polycarbonate thermal box, 5-line laser launch [405 (100 mW), 445 (45 mW), 488 (100 mW), 561 (80 mW), 640 (75 mW)], PRIME 95B Monochrome Digital Camera and 100×1.45 NA objective. Images were further edited with Adobe Photoshop 2023.

2′3′-cGAMP quantification

For intracellular and extracellular 2′3′-cGAMP quantification, 6–10 $\times 10^6$ of CT26 or 4–5 $\times 10^6$ of EO771.LMB or 4T1 cells were seeded into 15-cm dishes. If indicated in the Figure or Supplementary Figure, cells were administered one of the following treatments 24 hours after seeding: (i) cells were transfected with 8 μg of herring testes (HT)-DNA (Millipore Sigma) using Lipofectamine 3000 transfection reagent (Invitrogen) per the manufacturer's instructions; (ii) cells were treated with 5 μmol/L paclitaxel (Cayman Chemical) or DMSO control; (iii) cells were transfected with 1.2 μg of poly(I:C; Thermo Fisher Scientific) using Lipofectamine 3000 transfection reagent per the manufacturer's instructions. A total of 16 hours prior to media and/or cell collection, media were changed to serum-free red phenol-free RPMI (Corning), and paclitaxel treatment was replenished in the media. A total of 16 hours following media exchange, and no later than 24 hours after HT-DNA transfection or 48 hours after paclitaxel treatment, the conditioned media were removed and centrifuged at ≥ 600 × *g* at 4°C for 15 minutes. Supernatant was assayed directly using the 2′3′-cGAMP ELISA Kit (Arbor Assays) according to the manufacturer's instructions. All steps were performed on ice. Cells were harvested, washed with PBS and counted. Cells were then centrifuged at 500 × *g* at 4°C for 5 minutes. Whole-cell lysates were generated by lysing the cell pellet in LP2 lysis buffer [20 mmol/L Tris HCl pH 7.7, 100 mmol/L NaCl, 10 mmol/L NaF, 20 mmol/L β-glycerophosphate, 5 mmol/L $MgCl_2$, 0.1% (v/v) Triton X-100, 5% (v/v) Glycerol] and incubated on ice for 30 minutes. Lysates were sonicated using a Bioruptor 300 (Diagenode) on the high setting for five to 15 cycles 30 seconds ON/30 seconds OFF at 4°C. After centrifugation (21,000 × *g*, 20 minutes, 4°C), 2′3′-cGAMP levels were quantified using the 2′3′-cGAMP ELISA Kit according to the manufacturer's instructions.

IFNβ quantification

For secreted IFNβ quantification, 6–10 $\times 10^6$ of CT26 or 4–5 $\times 10^6$ of EO771.LMB or 4T1 cells were seeded into 15-cm dishes. If indicated in the Figure or Supplementary Figure, cells were treated with 5 μmol/L paclitaxel (Cayman Chemical) or DMSO control 24 hours after seeding. A total of 16 hours prior to media and cell collection, media were changed to serum-free red phenol-free RPMI (Corning), and

paclitaxel treatment was replenished in the media. A total of 16 hours following media exchange and no later than 48 hours after paclitaxel treatment, the conditioned media were removed and centrifuged at ≥ 600 × *g* at 4°C for 15 minutes. Supernatant was assayed directly. All steps were performed on ice. Cells were harvested and washed with PBS; cell counts were measured and used for normalization of IFNβ quantification. IFNβ levels in the supernatant were quantified using the LEGEND MAX Mouse IFNβ ELISA Kit (BioLegend) according to the manufacturer's instructions.

Immunoblotting

Cells were harvested by trypsinization and lysed in RIPA buffer (25 mmol/L Tris-HCl pH 7.6, 150 mmol/L NaCl, 1% NP-40, 1% sodium deoxycholate, 0.1% SDS, 0.5 mmol/L PMSF), supplemented with phosphatase inhibitors (10 mmol/L NaF, 20 mmol/L β-glycerophosphate) and protease inhibitor (Thermo Fisher Scientific) at approximately 10^7 cells/mL and incubated on ice for 20 minutes. Lysates were then sonicated using a Bioruptor 300 (Diagenode) on the high setting for 15 cycles 30 seconds ON/30 seconds OFF at 4°C, and reincubated on ice for 20 minutes. After centrifugation (21,000 × *g*, 20 minutes, 4°C), protein concentration of the supernatant was determined using bicinchoninic acid (BCA) protein assay (Thermo Fisher Scientific) and 25–50 μg of protein per sample was loaded on Tris-Glycine gels (Thermo Fisher Scientific).

Membranes were blocked in 5% milk in TBS with 0.1% Tween-20 (TBS-T) and incubated with primary antibody (anti-TREX1 CST76892 1:250; anti-cGAS CST31659 1:1,000; anti-STING CST50494 1:250; anti-TBK1 CST3504 1:1,000; anti-pTBK1 CST5483 1:250; anti-IRF3 CST4302 1:250; anti-pIRF3 CST4947 1:250; anti-β-actin ab8224 and ab8227 1:5,000; anti-α-tubulin ab7291 1:5,000) overnight at 4°C, washed four times in TBS-T, and incubated for 2 hours at room temperature with horseradish peroxidase (HRP)-conjugated secondary antibody (Thermo Fisher Scientific; Goat anti-Mouse IgG HRP 31432; Goat anti-Rabbit IgG HRP PI31462) at 1:10,000 dilutions in blocking buffer supplemented with 0.1% Tween. After four washes in TBS-T, membranes were rinsed in TBS and imaging was performed using enhanced chemiluminescence (Thermo Fisher Scientific).

For Western blot quantifications, membranes were blocked in Odyssey blocking buffer in TBS (LI-COR). Primary antibodies were diluted in blocking buffer supplemented with 0.2% Tween and incubated with membranes overnight at 4°C. Secondary antibodies (Thermo Fisher Scientific; Goat anti-Rabbit 680 PIA32734; Goat anti-Rabbit 800 PIA32735) were used at 1:20,000 dilutions in blocking buffer supplemented with 0.2% Tween. Fluorescence was measured using an infrared imaging scanner (Odyssey; LI-COR) according to the manufacturer's instructions.

Gene expression analysis

For the quantification of mRNA expression, total RNA was isolated from 1–2 × 10^6 cells using an RNeasy Plus Mini Kit (Qiagen), according to the manufacturer's instructions. cDNA was generated from 1–2 μg RNA using the High-Capacity cDNA Reverse Transcription Kit (Thermo Fisher Scientific) or the SuperScript IV first-strand synthesis system (Life Technologies), with random hexamer priming. Quantitative PCR was performed using the Applied Biosystems PowerUp SYBR Green Master Mix (Thermo Fisher Scientific) with detection on a QuantStudio6 (Applied Biosystems) cycler with gene specific primers (*Gapdh* forward AGGTCGGTGTGAACGGATTTG, reverse TGTAGACCATGTAGTTGAGGTCA; *Actin* forward GGCTGTATTCCCCTCCATCG, reverse CCAGTTGGTAACAATGCCATGT; *Isg54* forward GGGAAAGCAGAGGAAATCAA, reverse TGAAAGTTGCCATACAGAAG; *Isg56* forward CAGAAGCACACATTGAAGAA, reverse TGTAAGTAGCCAGAGGAAGG; *Ifnb1* forward GTCCTCAACTGCTCTCCACT, reverse CCTGCAACCACCACTCATTC; *Trex1* forward TCCAGACAGAGCTTGCTAGG, reverse ATGTGAGTCTGTCGGTGCTT). At least three biological replicates were conducted for each experiment. Relative transcription levels were calculated by normalizing to both *Gapdh* and *Actin* expression levels using the ΔΔCt method.

3′→5′ exonuclease activity assay

For nuclease activity assessment, 3–5 × 10^6 EO771.LMB cells were resuspended in 80 μL of assay buffer (25 mmol/L HEPES pH 7.5, 20 mmol/L KCl, 1 mmol/L DTT, 1% Triton X-100, 0.25 mmol/L EDTA, 10 mmol/L $MgCl_2$) supplemented with Complete Mini Protease Inhibitor Cocktail (Roche). Cells were lysed by passing the resuspension through a 28G needle (BD Biosciences) 10 times. After centrifugation (14,000 × *g*, 15 minutes, 4°C), the protein concentration of each supernatant was determined using Reducing Agent Compatible BCA protein assay (Thermo Fisher Scientific) according to the manufacturer's instructions. Oligonucleotides for generating the dsDNA substrate (oligo 1: /5TEX615/GCTAGGCAG, oligo 2: CTGCCTAGC/3IAbRQSp/) were purchased from Integrated DNA Technologies (IDT). A 1:1.15 mixture of oligo 1 and oligo 2 was annealed by heating at 94°C for 2 minutes and gradually cooling to room temperature. Four technical replicates of each sample were loaded onto a 384-well F-bottom microplate (Greiner Bio-One International). Each reaction contained 4–25 μg of total proteins (20 μg of CT26 proteins, 4 μg of EO771.LMB proteins, and 25 μg of 4T1 proteins) and 1,000 nmol/L of the dsDNA substrate in a total of 20 μL assay buffer. For the negative control (buffer-only), 1,000 nmol/L of the dsDNA substrate in 20 μL pure assay buffer was used. Immediately after the addition of the dsDNA substrate, the fluorescence was recorded every 3 minutes for 120 minutes, at 26°C (615 nm emission, 570 nm excitation) on a Cytation 3 Plate Reader with Gen5 Software (BioTek).

Confluence experiments

For confluency measurements, 6,000 CT26, EO771.LMB, or 4T1 cultured cells were seeded in triplicate in 24-well plates. Growth over time was then measured by calculating daily cell confluency using an IncuCyte Live-Cell Analysis Imager (Essen/Sartorius). The IncuCyte takes images of each well and analyzes them by applying a predetermined mask to each image that distinguishes between an empty surface and a surface covered by cells. Once the mask has been applied, the program calculates the surface area occupied by cells and the percentage confluency. Images were taken every 12–24 hours and technical replicates were averaged to generate the percentage confluence, which was then plotted across time to generate growth curves. Final growth curves represent data from three independent biological replicates.

Animals

Animal experiments were performed in accordance with protocols approved by the MSKCC Institutional Animal Care and Use Committee. All mice used in the *in vivo* experiments were female. Experiments were initiated when animals were 7–8 weeks of age. There was no need to randomize animals. Investigators were not blinded to group allocation. C57BL/6J wild-type (stock no. 000664), *Rag1*$^{-/-}$ (stock no. 002216), NU/J (stock no. 002019), *Ifnar1*$^{-/-}$ (stock no. 028288), and BALB/C (stock no. 000651) strains were all purchased from the Jackson Laboratory.

Tumor growth and survival analyses

For CT26 inoculation, 2×10^5 cells were resuspended in 50 μL PBS mixed with 30% Matrigel (BD Biosciences) and injected into the right flank of mice. Only one tumor was implanted per animal.

For orthotopic mammary fat pad implantation of EO771.LMB or 4T1 tumor cells, 2×10^5 EO771.LMB cells were resuspended in 50 μL Hank's Balanced Salt Solution (Thermo Fisher Scientific) and 2×10^5 4T1 cells were resuspended in 50 μL PBS mixed 1:1 with Matrigel. Cells were kept on ice until implanted in the animals. Mice were anesthetized using inhalation of isoflurane (2.5%). The depth of anesthesia was confirmed by verifying absence of toe pinch response. An incision was made in the right flank, and tumor cells were injected into the fourth mammary fat pad. Only one tumor was implanted per animal. The wound was closed using two to three wound clips. All animals were given meloxicam (2 mg/kg) every 24 hours to alleviate pain for 2 days after orthotopic surgery.

For all *in vivo* studies, 10–15 mice per study were used, and primary tumor growth and overall survival were monitored every 2–3 days, for up to 120 days after tumor implantation. The length (L) and width (W) of the tumor were measured using calipers. The tumor size was calculated according to the following formula: $(L \times W^2)/2$. Endpoint was determined when the primary tumor reached the size of 2,000 mm^3.

Animal immunotherapy experiments

For the immunotherapy animal experiments, tumor cells were orthotopically implanted in the mammary fat pad, as described above. A total of 200 μg of rat anti-mouse PD-1 IgG2a antibody (BioXCell BE0273-A050), or its corresponding isotype control antibody (BioXCell BE0089-A050), were delivered intraperitoneally in 100 μL of PBS to mice 6, 9, 12, and 15 days after tumor implantation. Animals were monitored for tumor growth and overall survival for up to 120 days.

Animal IFN signaling blockade experiments

For the type I IFN signaling blockade animal experiment, tumor cells were subcutaneously injected in the right flank, as described above. 1,000 μg (5×) of anti-mouse IFNAR-1 IgG1 antibody (BioXCell BE0241; clone MAR1-53A), or its corresponding isotype control antibody (BioXCell BE0083; clone MOPC-21), were delivered intraperitoneally in 200 μL of PBS to mice, 1 day prior to tumor injection to deplete animals from IFN signaling. Type I IFN signaling blockade was maintained throughout the length of the experiments by delivering 200 μg (1×) of anti-mouse IFNAR-1 IgG1 antibody, or its corresponding isotype control antibody, in 50 μL of PBS to mice once a week. Animals were monitored for tumor growth and overall survival for up to 120 days.

Immune phenotyping of solid tumors

For immune profiling, single-cell suspensions were prepared from isolated tumors as described previously (41). Briefly, animals were sacrificed 10, 15, or 16 days after tumor implantation, and primary tumors were collected. Tumor tissue was minced into pieces of 1–2 mm and digested with collagenase (Millipore Sigma) and hyaluronidase (Millipore Sigma) in DMEM supplemented with 5% FBS for 30 minutes at 37°C. After centrifugation (200 × *g*, 5 minutes, 4°C), cell suspensions were successively digested in DNase I (Roche), trypsin (Gibco), and Dispase II (Roche). The samples were then lysed in red blood cell lysis buffer (Thermo Fisher Scientific) to remove red blood cells. The final single-cell suspensions were resuspended in PBS supplemented with 2% FBS and passed through a 70-μm cell strainer (Falcon). Single-cell suspensions were stained with a mixture of fluorochrome-conjugated antibodies (anti-CD45 103108; anti-CD4 100432; anti-CD8 140408; anti-CD279/PD-1 135224; anti-CD19 115523; anti-GranzymeB 396410; anti-NK1.1 156506; all antibodies from Biolegend) and DAPI (Thermo Fisher Scientific) for 20–30 minutes in the dark at 4°C, washed twice, and resuspended in fresh PBS supplemented with 2% FBS. Data were acquired on a Cytek Aurora flow cytometer using SpectroFLO software. Compensation and data analysis were performed using FlowJo software 10.8.2. Unstained biological controls and single-color controls were used. Cell populations were identified using sequential gating strategy.

Statistical analysis

GraphPad Prism 10.1.1 (270) was used to statistically analyze the data generated in this study. As indicated in the Figure and Supplementary Figure legends, the statistical methods used were either one-sided or two-sided *t* tests and one-way or two-way ANOVA (for bar graph analyses, tumor growth curves, and exonuclease assay analyses), log-rank test (for *in vivo* survival analyses) or two-sided Mann–Whitney test (for flow cytometry analyses). The *P* value thresholds for all analyses were: *, $P < 0.05$; **, $P < 0.01$; ***, $P < 0.001$; and ****, $P < 0.0001$. Detailed Information regarding biological replicates, sample size, and statistical testing for each individual experiment is provided in the figure legends.

Data availability

The data generated in this study are available in the article and its Supplementary Data and the raw data are available upon request from the corresponding author.

Results

CIN results in cGAS-STING-dependent TREX1 induction

To identify adaptive mechanisms that promote tolerance of cytosolic DNA in cells with CIN, we selected three syngeneic mouse models for study, including one colorectal carcinoma (CT26) and two triple-negative breast cancer (TNBC; EO771.LMB and 4T1) models. Consistent with our previous results (24, 26), all three models exhibited evidence of CIN, including micronuclei in approximately 8%–11% of cells (**Fig. 1A** and **B**). Moreover, cGAS and STING expression were maintained in all three models and cGAS accumulated in 12%–35% of micronuclei, indicating frequent micronuclear envelope rupture (**Fig. 1C** and **D**). Nevertheless, ELISA analysis revealed low to undetectable amounts of cGAMP in CT26 (7 ± 4 SD fmol/million cells) and EO771.LMB (13 ± 7 SD fmol/million cells) cell lysates; these levels were either lower or not significantly different compared with cGAMP levels in *Cgas* KO lysates (CT26 *Cgas* KO: 14 ± 1 SD fmol/million cells; EO771.LMB *Cgas* KO: 7 ± 3 SD fmol/million cells; **Fig. 1E**; Supplementary Fig. S1A and S1B). In contrast, wild-type 4T1 lysates exhibited modest increases in cGAMP (10 ± 4 SD fmol/million cells) relative to 4T1 *Cgas* KO lysates (3 ± 3 SD fmol/million cells; **Fig. 1E**; Supplementary Fig. S1C). Low levels of cGAMP were also detected in conditioned media collected from CT26, EO771.LMB, and 4T1 cultures, indicating that cGAMP was exported, as reported previously (Supplementary Fig. S1D; ref. 42). Transfection with HT-DNA resulted in strong increases in cGAMP, further confirming that upstream cytosolic DNA sensing—cGAS activation by cytosolic DNA—is intact in all three models (Supplementary Fig. S1E and S1F).

Further characterization of *Cgas* KO cells led to the observation that CT26 and EO771.LMB *Cgas* KO cells possessed significantly diminished TREX1 protein levels relative to their wild-type counterparts

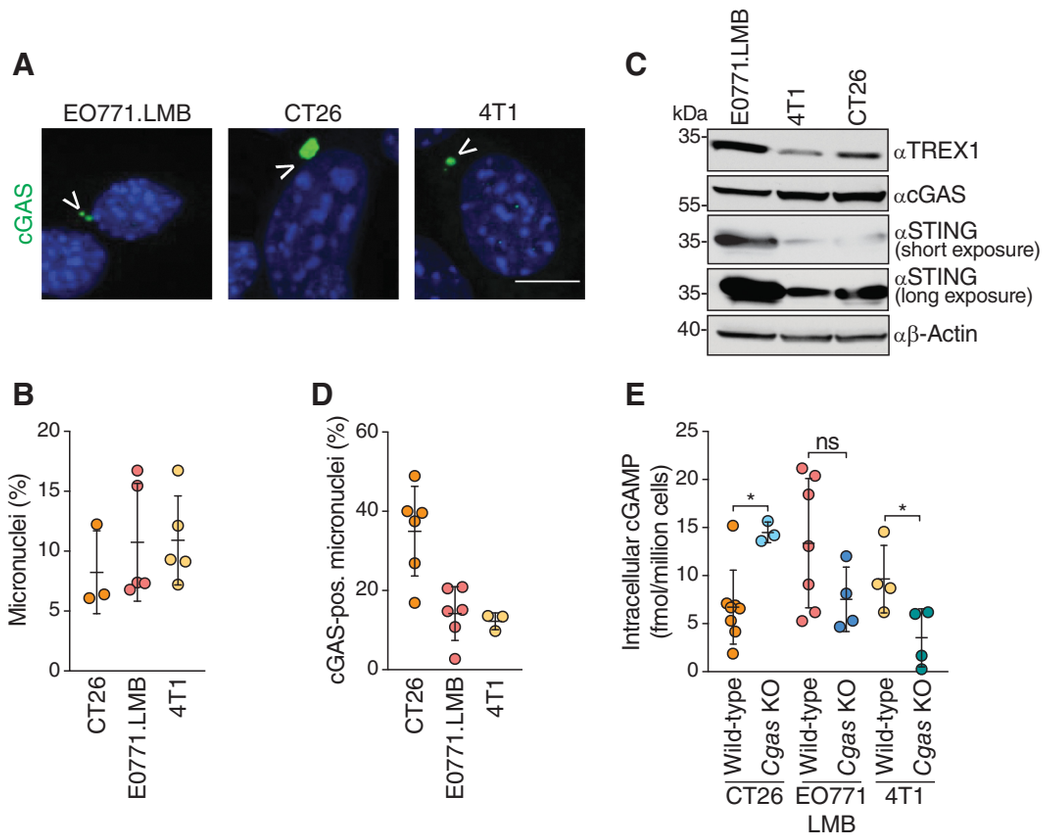

Figure 1.

Chromosomally unstable cancer cells exhibit modest cGAMP accumulation. **A,** Immunofluorescence for cGAS (green) in the indicated cells. Arrowheads denote micronuclei. DNA was stained with Hoechst 33342. Scale bars = 10 μm. **B,** Quantification of the frequency of micronuclei in the indicated cells as in **A**; mean ± SD, n = 3–5 experiments (>200 cells analyzed per experiment). **C,** Immunoblotting for cGAS, STING, TREX1, and β-actin in the indicated cells. **D,** Quantification of the frequency of cGAS-positive micronuclei in the indicated cells as in **A**; mean ± SD, n = 3–5 experiments (>200 cells analyzed per experiment). **E,** ELISA analysis of intracellular cGAMP production in the indicated cells; mean ± SD, n = 4–8 biological replicates. One-sided t test was used to determine statistical significance; *, $P < 0.05$; ns, not significant.

(**Fig. 2A**–**B** and **D**). TREX1 levels were similarly decreased upon *Sting1* deletion in EO771.LMB cells (**Fig. 2B** and **D**). Stimulation via HT-DNA transfection led to cGAS-dependent increases in TREX1 protein levels in CT26 and EO771.LMB cells (Supplementary Fig. S2A and S2B). *Cgas* deletion did not impact TREX1 protein levels in 4T1 cells or in chromosomally stable MCF10A human mammary epithelial cells (**Fig. 2C** and **D**; Supplementary Fig. S2C–S2E). TREX1 levels in 4T1 cells were unaffected following stimulation with HT-DNA (Supplementary Fig. S2C). These data suggest that *Trex1* mRNA may be upregulated downstream of cGAS-STING activation in a subset of cancer cell lines.

Prior reports have documented *Trex1* induction by treatment with genotoxic agents or by exposure of macrophages and dendritic cells to inflammatory stimuli, such as Toll-like receptor ligands, but roles for cGAS-STING in driving *Trex1* expression in cancer cells have not been described previously (43–45). To investigate this possibility, we used real-time quantitative PCR to determine whether increases in TREX1 protein were derived from cGAS-STING–dependent transcriptional upregulation of *Trex1* mRNA. Indeed, *Trex1* mRNA levels were decreased approximately 5× in *Cgas* and *Sting1* KO EO771.LMB cells and 2.5× *Cgas* KO CT26 cells relative to wild-type controls (**Fig. 2E**). Consistent with results at the protein level, *Cgas* deletion did not substantially reduce *Trex1* mRNA levels in 4T1 cells (**Fig. 2E**). Together, these data indicate that chronic cGAS-STING activation results in upregulation of TREX1 mRNA and protein in a subset of mouse colorectal carcinoma and TNBC cells.

To better understand the impact of *Trex1* transcriptional upregulation, we assayed TREX1 exonuclease activity in cell lysates. In brief, lysates were incubated with a dsDNA substrate with a fluorescent label at one 5′ end closely positioned next to a 3′ quencher (**Fig. 2F**). TREX1 3′→5′ exonuclease activity is predicted to free the fluorescent dye and thus result in the acquisition of fluorescence. Incubation of this probe in wild-type cell lysates resulted in rapid acquisition of fluorescence (**Fig. 2G**; Supplementary Fig. S2F and S2G). *Trex1* deletion severely diminished acquisition of fluorescence, confirming the specificity of this assay for TREX1 exonuclease activity (**Fig. 2G**; Supplementary Fig. S2F and S2G). Lysates prepared from *Cgas* KO CT26 and EO771.LMB cells, but not *Cgas* KO 4T1 cells, exhibited significant decreases in fluorescence compared with wild-type controls, confirming that *Trex1* transcriptional upregulation translates into a corresponding increase in exonuclease activity (**Fig. 2G**; Supplementary Fig. S2F and S2G). Together, these results suggest that TREX1 upregulation may inhibit cGAS-STING activation within chromosomally unstable cancer cells.

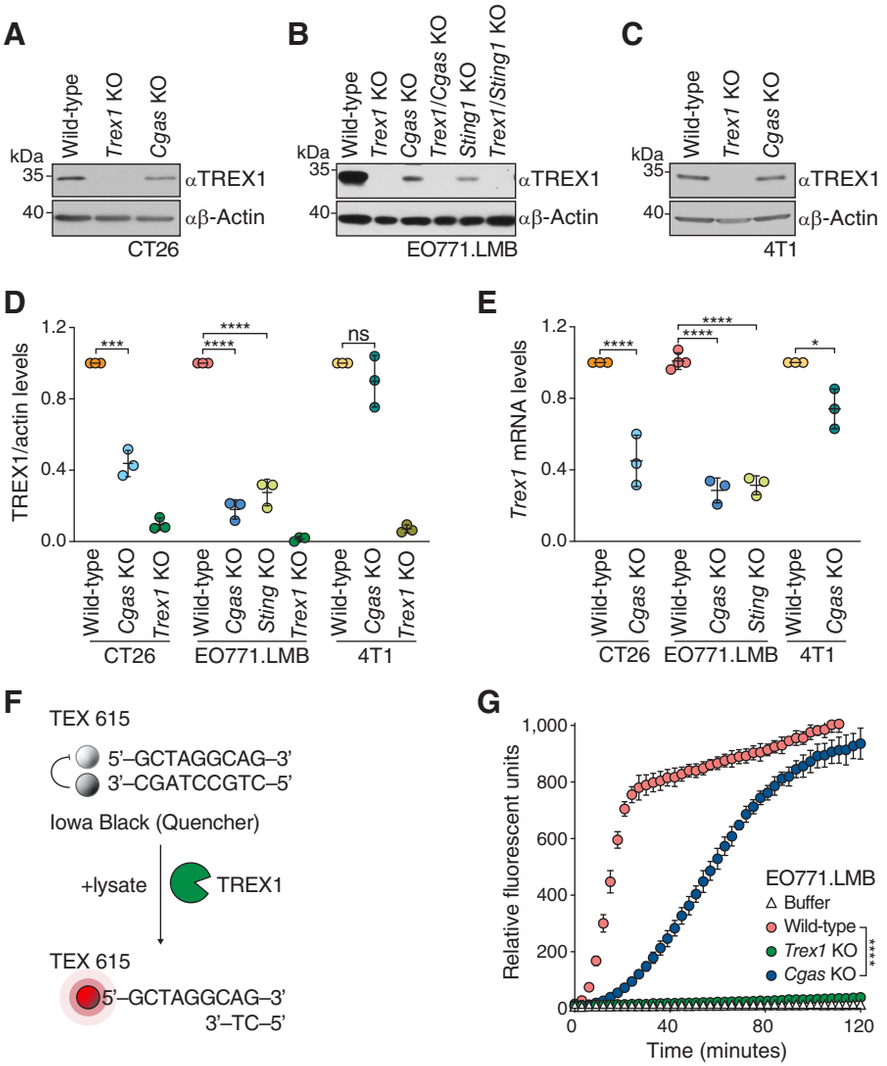

Figure 2.
CIN drives cGAS-STING–dependent TREX1 upregulation. Immunoblotting for TREX1 and β-actin in the indicated CT26 (**A**), EO771.LMB (**B**), and 4T1 (**C**) cells. **D,** Quantification of TREX1 relative to corresponding β-actin signal in the indicated cell lines as shown in **A–C**; mean ± SD, $n = 3$ experiments. Two-sided *t* test was used to determine statistical significance; ****, $P < 0.0001$; ***, $P < 0.001$, ns, not significant. **E,** qRT-PCR of *Trex1* expression in the indicated cell lines; mean ± SD, $n = 3$–4 technical replicates. Two-sided *t* test was used to determine statistical significance; ****, $P < 0.0001$; *, $P < 0.05$. **F,** Schematic representation of the *in vitro* assay for TREX1 exonuclease activity. A dsDNA substrate with a 5′ TEX615 fluorophore and an adjacent Iowa Black quencher is incubated with cell lysate. TREX1 exonuclease activity liberates TEX615 fluorescence by eliminating Iowa Black quenching. **G,** Time course of TREX1 exonuclease activity on dsDNA substrate as in **F**; mean ± SD, representative example from $n = 3$ experiments. One-way ANOVA was used to determine statistical significance; ****, $P < 0.0001$.

TREX1 induction blocks cGAS-STING activation

To determine if TREX1 dampens cGAS activation in chromosomally unstable cancer cells, we measured cGAMP levels using ELISA. *Trex1* KO cells exhibited significant 3–4× increases in cGAMP compared with wild-type controls, accumulating 33 ± 17 SD fmol of cGAMP per million cells in CT26 lysates, 44 ± 23 SD fmol of cGAMP per million cells in EO771.LMB lysates, and 42 ± 20 SD fmol of cGAMP per million cells in 4T1 lysates (**Fig. 3A–C**). Media collected from *Trex1* KO cultures contained 65±19 SD fmol of cGAMP per million CT26 cells, 50 ± 1 SD fmol of cGAMP per million EO771.LMB cells, and 171 ± 42 SD fmol of cGAMP per million 4T1 cells, approximately 2–3× increases compared to their respective wild-type controls (**Fig. 3D–F**). Higher levels of extracellular cGAMP in the 4T1 model, both at baseline and upon *Trex1* deletion, may reflect more efficient cGAMP export (46). Increased cGAMP levels in the *Trex1* KO cells could not be explained by variations in micronucleation or micronuclear envelope rupturing (Supplementary Fig. S3A–S3C). In EO771.LMB cells, *Trex1* deficiency was associated with evidence of downstream cGAS-STING pathway activation, including increased TBK1 S172 and IRF3 S396 phosphorylation (**Fig. 3G**). Together, these data indicate that TREX1 restrains cGAS-STING activation in chromosomally unstable cancer cells.

Exacerbating CIN by paclitaxel treatment significantly increased cGAMP production in EO771.LMB *Trex1* KO cells compared with wild-type controls (114 ± 12 SD fmol cGAMP per million wild-type cells vs. 259 ± 88 SD fmol cGAMP per million *Trex1* KO cells; Supplementary Fig. S4A–S4C). In addition, paclitaxel treatment led to increases in TREX1 protein levels (Supplementary Fig. S4D and S4E). These observations suggest that TREX1 induction by genotoxic therapies may limit the ability of such therapies to activate cGAS-STING signaling.

TREX1 induction promotes tumor growth

To assess the role of TREX1 induction *in vivo*, we transplanted wild-type and *Trex1* KO CT26 tumors in immunocompetent BALB/c mice. Loss of *Trex1* led to marked reductions in primary tumor growth (37 ± 54 SD mm^3 in *Trex1* KO tumors vs. 1,307 ± 713 SD mm^3 in wild-type tumors at 24 days posttransplantation; **Fig. 4A**; Supplementary Fig. S5A). In contrast to the 28 days median survival of animals transplanted with wild-type CT26 tumors, animals transplanted with *Trex1* KO CT26 tumors exhibited a longer median survival of 45 days (**Fig. 4B**). Fifty-seven percent of animals bearing *Trex1* KO tumors were tumor-free 120 days after tumor injection, compared with 0% of

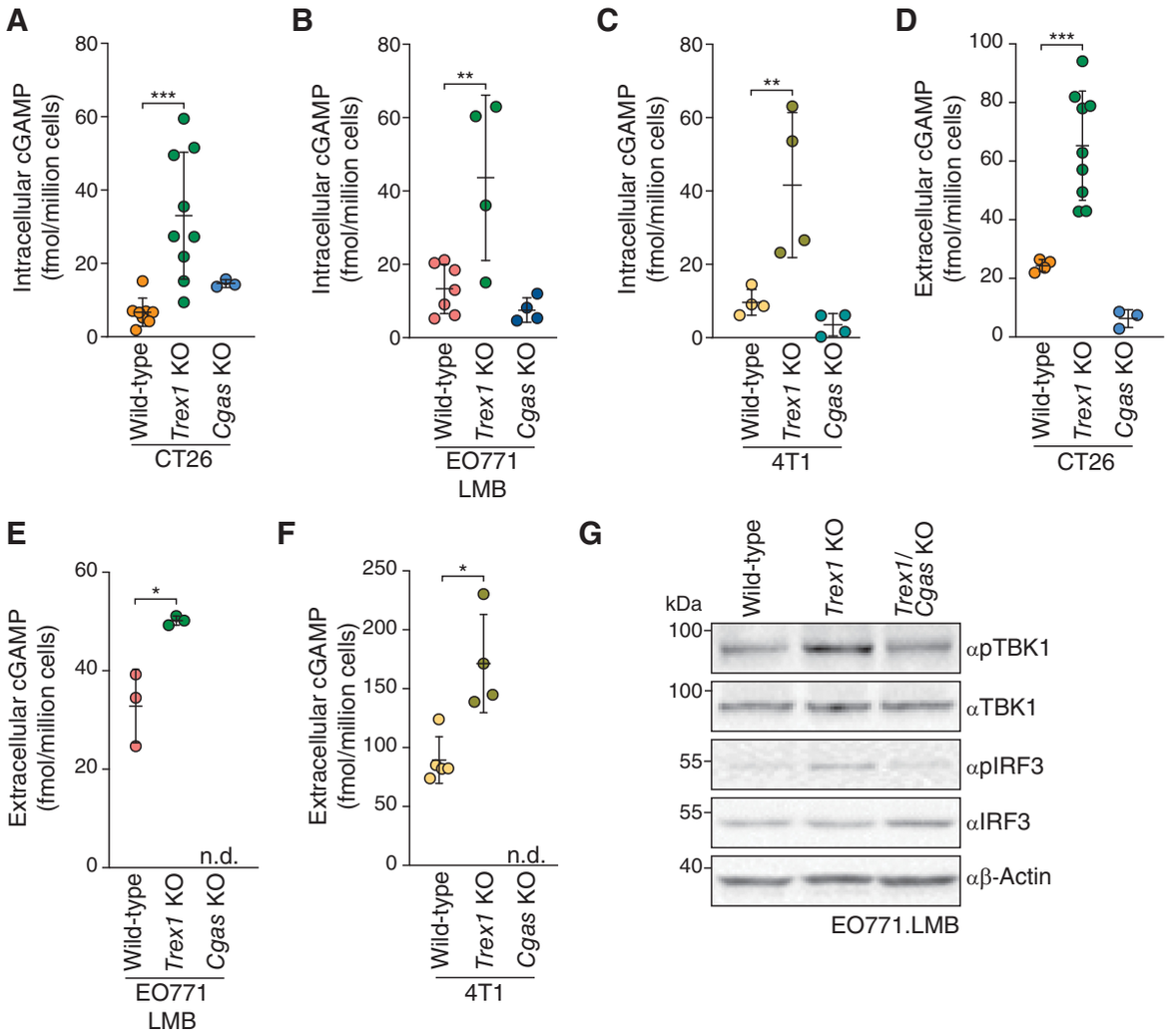

Figure 3.

TREX1 induction limits cGAS-STING activation in chromosomally unstable cancer cells. ELISA analysis of intracellular cGAMP production in the indicated CT26 (**A**), EO771.LMB (**B**), and 4T1 (**C**) cells; mean ± SD, $n = 4$–8 biological replicates. One-way ANOVA was used to determine statistical significance; ***, $P < 0.001$; **, $P < 0.01$. ELISA analysis of extracellular cGAMP production in the indicated CT26 (**D**), EO771.LMB (**E**), and 4T1 (**F**) cells; mean ± SD, $n = 4$–8 biological replicates, nd, not detected. One-way ANOVA was used to determine statistical significance; ***, $P < 0.001$; *, $P < 0.05$. **G,** Immunoblotting for TBK1, phospho-TBK1(S172), IRF3, phospho-IRF3 (S396) and β-actin in the indicated EO771.LMB cells.

animals bearing wild-type tumors. To further assess how TREX1 induction affects tumor growth, we orthotopically transplanted wild-type and *Trex1* KO EO771.LMB cells into the mammary fat pad of C57BL/6J mice. Similar to results in the CT26 model, *Trex1*-deficient EO771.LMB tumors exhibited significant reductions in primary tumor growth (118 ± 111 SD mm^3 in *Trex1* KO tumors vs. 512±382 SD mm^3 in wild-type tumors at 18 days posttransplantation; **Fig. 4C**; Supplementary Fig. S5B and S5C). In contrast to the 23.5 days median survival of animals transplanted with wild-type EO771.LMB cells, animals transplanted with *Trex1* KO EO771.LMB cells exhibited a longer median survival of 39 days (**Fig. 4D**; Supplementary Fig. S5D).

Differences in tumor growth and overall survival could not be explained by alterations in the cellular proliferation of *Trex1* KO cells (Supplementary Fig. S5E and S5F). Tumor growth reductions seen in *Trex1* KOs were fully rescued with concomitant loss of *Cgas* or *Sting1* in EO771.LMB tumors (**Fig. 4C**; Supplementary Fig. S5B and S5C). Co-deletion of *Cgas* and *Sting1* also erased the survival benefit associated with intratumoral TREX1 loss (**Fig. 4D**; Supplementary Fig. S5D). As reported previously, *Cgas* loss modestly delayed tumor growth and extended host survival (Supplementary Fig. S5B–S5D; refs. 24, 47). In contrast, *Sting1* deletion accelerated tumor growth, likely reflecting the loss of a baseline proinflammatory transcriptional response that is further elevated upon *Trex1* deletion (Supplementary Fig. S5B and S5C).

In contrast to the results in CT26 and EO771.LMB cells, loss of TREX1 offered modest benefit in the 4T1 model. *Trex1* deletion led to a mild reduction in tumor growth and extension of overall survival; however, intratumoral cGAS expression was dispensable for these effects (**Fig. 4E** and **F**; Supplementary Fig. S5G). Reduction in tumor growth was not associated with alterations in cellular proliferation

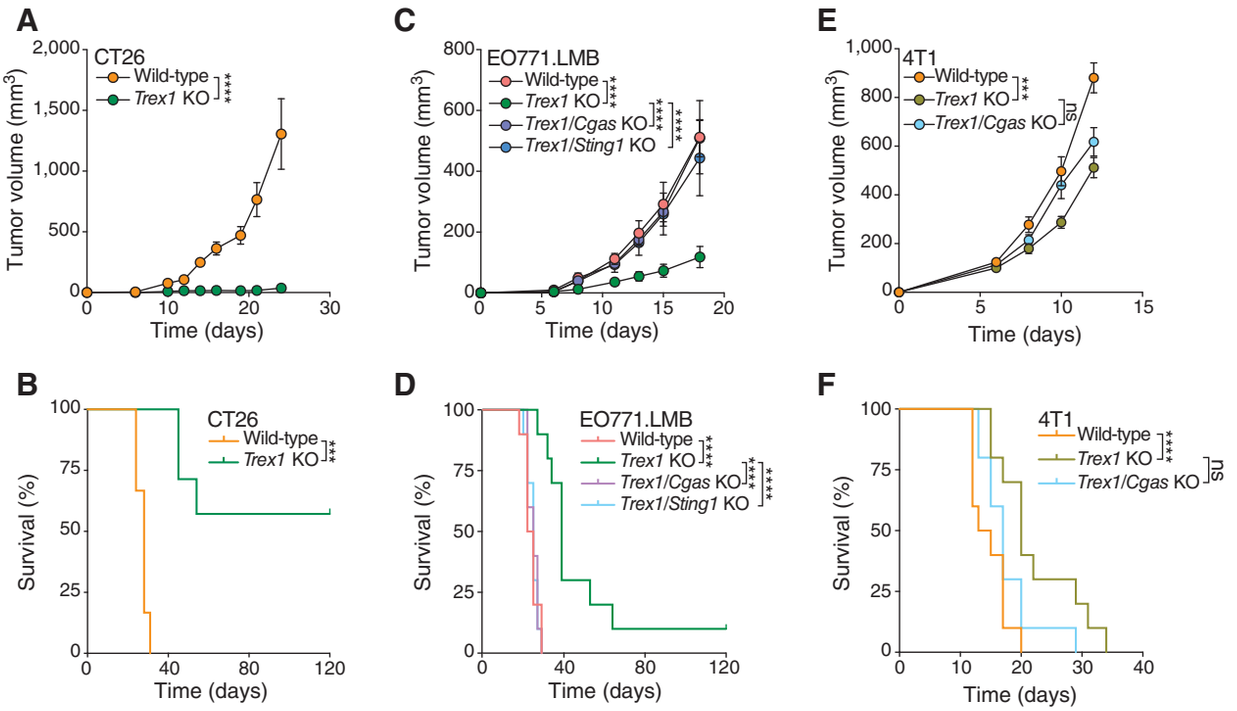

Figure 4.

TREX1 induction promotes tumor growth. **A,** Growth curves of indicated injected CT26 tumors; datapoints, mean ± SEM, $n = 6$–7 animals per group. **B,** Survival of BALB/c animals after injection with indicated CT26 tumor cells; $n = 6$–7 animals per group. **C,** Growth curves of indicated orthotopically transplanted EO771.LMB tumors; datapoints, mean ± SEM, $n = 10$ animals per group. **D,** Survival of C57BL/6J animals after orthotopic transplantation with indicated EO771.LMB tumor cells; $n = 10$ animals per group. **E,** Growth curves of indicated orthotopically transplanted 4T1 tumors; datapoints, mean ± SEM, $n = 10$ animals per group. **F,** Survival of BALB/c animals after orthotopic transplantation with indicated 4T1 tumor cells; $n = 10$ animals per group. Two-sided t test was used to determine statistical significance at the last timepoint in **A**, **C**, and **E**; ****, $P < 0.0001$; ***, $P < 0.001$, ns, not significant. log-rank test was used to determine statistical significance in **B**, **D**, and **F**; ****, $P < 0.0001$; ***, $P < 0.001$; ns, not significant.

(Supplementary Fig. S5H). Taken together, these experiments suggest that intratumoral TREX1 loss significantly reduces tumor growth in a cGAS-STING–dependent manner within a subset of chromosomally unstable cancer cells.

TREX1 induction curbs antitumor immunity

cGAS-STING signaling can drive tumor regression via an enhanced antitumor immune response (48, 49). Therefore, we next used flow cytometry to characterize the impact of TREX1 loss on tumor immune infiltration. Immune profiling of *Trex1* KO EO771.LMB tumors harvested 10–16 days after transplantation revealed significant increases in $CD45^+$ cells, $CD4^+$ T cells and $CD19^+$ B cells relative to wild-type and *Trex1/Cgas* KO controls (**Fig. 5A**; Supplementary Fig. S6A and S6B). $CD4^+$ and $CD8^+$ T cells present in *Trex1* KO tumors exhibited higher levels of PD-1 expression, suggestive of a larger pool of tumor-reactive cells (**Fig. 5A**; ref. 50). We did not detect any differences in the proportions of Granzyme B^+ $CD8^+$ T cells or $NK1.1^+$ cells within *Trex1* KO tumors (Supplementary Fig. S6C). Unlike EO771.LMB tumors, immune profiling of the 4T1 model did not reveal any significant differences in immune cell infiltration between wild-type and *Trex1* KO tumors across multiple timepoints posttransplantation (Supplementary Fig. S6D and S6E).

To more directly assess a potential role for host adaptive immunity in the diminished growth of *Trex1* KO tumors, we orthotopically transplanted parental and *Trex1* KO EO771.LMB cells into the mammary fat pads of *Rag1* KO mice, which are T and B cell–deficient and therefore immunocompromised (**Fig. 5B**). In contrast to the results obtained in immunocompetent animals, wild-type and *Trex1* KO tumors grew at similar rates in this setting (**Fig. 5B**; Supplementary Fig. S7A). Consistent with these results, intratumoral TREX1 loss failed to improve the overall survival of *Rag1* KO mice (**Fig. 5C**). Similar results were obtained in NU/J mice, which retain B-cell and natural killer–cell responses (**Fig. 5D** and **E**; Supplementary Fig. S7B). Taken together, these results indicate that TREX1 induction helps to shield chromosomally unstable cancers from host immunosurveillance.

TREX1 loss increases the efficacy of immune checkpoint blockade

Given the heightened immune response against *Trex1* KO tumors, we reasoned that intratumoral targeting of TREX1 may offer a therapeutic opportunity to further sensitize chromosomally unstable tumors to immune checkpoint blockade therapy. EO771.LMB and 4T1 cells were orthotopically transplanted into mammary fat pads of immunocompetent mice, and primary tumor growth was assessed (**Fig. 6A** and **B**). Animals were treated with four doses of anti-PD-1 immune checkpoint blockade starting 6 days after tumor inoculation. *Trex1* KO EO771.LMB tumors exhibited significantly reduced growth rates compared with their wild-type counterparts when both were treated with anti-PD-1 therapy, leading to significantly prolonged overall survival (**Fig. 6A** and **C**; Supplementary Fig. S8A). Sixty-seven percent of animals bearing EO771.LMB *Trex1* KO tumors were tumor-free 120 days after tumor inoculation, compared with 10% of wild-type

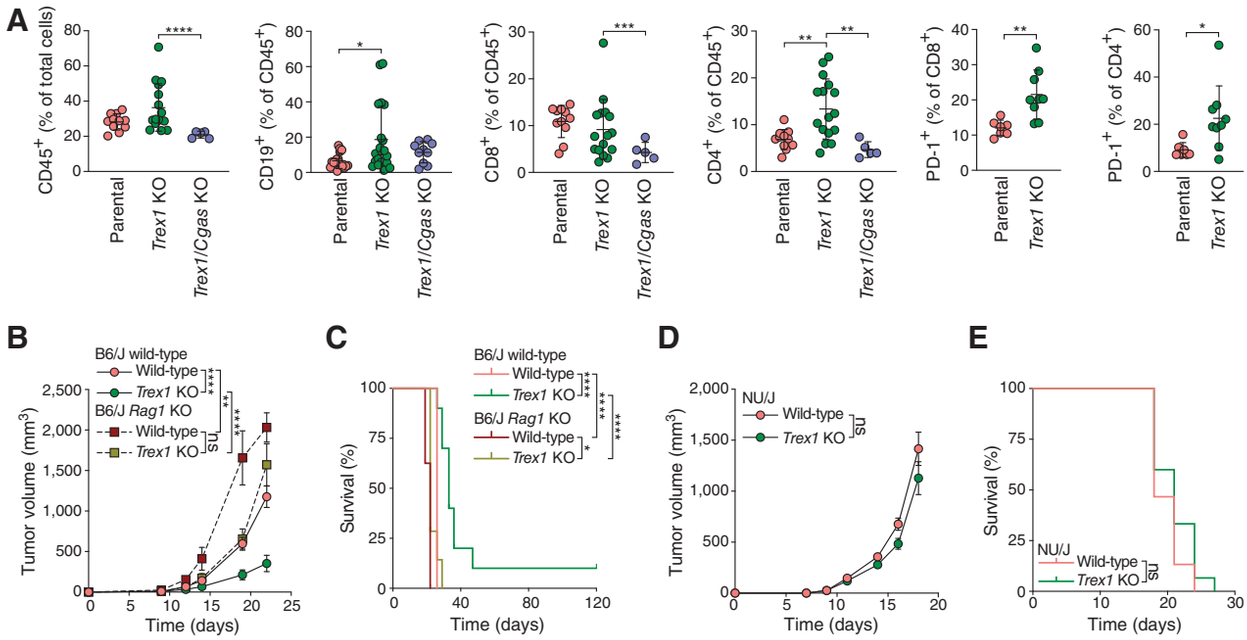

Figure 5.

TREX1 induction facilitates immune evasion. **A,** Immune infiltration analysis by flow cytometry in indicated tumors, collected from animals at 10 or 16 days posttransplantation of EO771.LMB tumor cells. Percentage of $CD45^+$ cells out of the total cells (day 16), percentage of $CD4^+$ (day 16), $CD8^+$ (day 10), and $CD19^+$ (day 16) cells out of $CD45^+$ cells, percentage of $PD\text{-}1^+$ cells out of $CD4^+$ (day 16) cells and percentage of $PD\text{-}1^+$ cells out of $CD8^+$ (day 16) cells obtained from dissociated tumors; mean ± SD, $n = 5$–16 tumors per group. Two-sided Mann–Whitney test was used to determine statistical significance; ****, $P < 0.0001$; ***, $P < 0.001$; **, $P < 0.01$; *, $P < 0.05$. **B,** Growth curves of indicated orthotopically transplanted EO771.LMB tumors into the mammary fat pad of C57BL/6J wild-type or *Rag1* KO mice; datapoints, mean ± SEM, $n = 7$–10 animals per group. **C,** Survival of C57BL/6J wild-type or *Rag1* KO animals after orthotopic transplantation with indicated EO771.LMB tumor cells; $n = 7$–10 animals per group. **D,** Growth curves of indicated orthotopically transplanted EO771.LMB tumors; datapoints, mean ± SEM, $n = 15$ animals per group. **E,** Survival of NU/J animals after orthotopic transplantation with indicated EO771.LMB tumor cells; $n = 15$ animals per group. Two-sided *t* test was used to determine statistical significance at the last timepoint in **B** and **D**; ****, $P < 0.0001$; **, $P < 0.01$; ns, not significant. log-rank test was used to determine statistical significance in **C** and **E**; ****, $P < 0.0001$; *, $P < 0.05$; ns, not significant.

tumor-bearing animals. In contrast, anti-PD-1 treatment failed to further diminish tumor growth or provide any survival benefit in the 4T1 model upon *Trex1* deletion (**Fig. 6B** and **D**; Supplementary Fig. S8B). Collectively, these results suggest that TREX1 inhibition is an attractive therapeutic strategy to potentiate responses to immune checkpoint blockade.

TREX1 induction promotes tumor growth by suppressing type I IFN

We next characterized downstream cGAS-STING signaling to better understand why *Trex1* deficiency led to diminished tumor growth and improved antitumor immunity in some cancer models (CT26, EO771.LMB), but not others (4T1). ELISA analysis of conditioned media collected from CT26 and EO771.LMB *Trex1* KO cultures identified significant increases in IFNβ relative to wild-type and *Cgas* KO control cells (4 ± 4 SD pg IFNβ per million wild-type CT26 cells vs. 31 ± 18 SD pg IFNβ per million *Trex1* KO CT26 cells; 24 ± 8 SD pg IFNβ per million wild-type EO771.LMB cells vs. 161 ± 2 SD pg IFNβ per million *Trex1* KO EO771.LMB cells; **Fig. 7A**). Transfection with HT-DNA resulted in strong increases in IFNβ in wild-type CT26 and EO771.LMB cells (24 ± 8 SD pg IFNβ per million wild-type CT26 untreated cells vs. 1002 ± 123 SD pg IFNβ per million cells +HT-DNA; 4±4 SD pg IFNβ per million wild-type EO771.LMB untreated cells vs. 202±66 SD pg IFN-β per million cells +HT-DNA; Supplementary Fig. S9A). Paclitaxel treatment further increased IFNβ production in EO771.LMB *Trex1* KO cells compared with wild-type controls (29±20 SD pg IFNβ per million wild-type cells vs. 395 ± 86 SD pg IFNβ per million *Trex1* KO cells; Supplementary Fig. S9B).

In contrast, despite accumulating similar levels of cGAMP, IFNβ was not detected in 4T1 cultures, even following *Trex1* deletion, indicating an apparent signaling defect downstream of cGAS-STING (**Fig. 7A**). Further examination confirmed that mRNA levels of *Ifnb1*, the gene coding for IFNβ, and interferon stimulated genes (ISG), such as *Isg54* and *Isg56*, are present at similar levels in wild-type and *Cgas* KO 4T1 cells, even following stimulation with HT-DNA (Supplementary Fig. S9C). In contrast, transfection of poly(I:C), a cGAS-STING–independent immunostimulant, resulted in a 1,000× increase in *Ifnb1* and 10–100× increases in *Isg54* and *Isg56* (Supplementary Fig. S9C). Taken together, these data indicate that 4T1 cells fail to translate increased cGAS activity to the induction of proinflammatory genes regardless of STING signaling strength. This suggests that the inherent ability to mount an IFN response downstream of cGAS-STING may be a critical component of the diminished tumor growth and the extension of overall survival observed upon intratumoral *Trex1* deletion.

IRF3 dimerization and nuclear translocation play critical roles in gene expression of type I IFN, associated ISGs, and other inflammatory mediators downstream of cGAS-STING activation (17, 51). We therefore generated EO771.LMB *Irf3* KO cells to better understand how downstream cGAS-STING signaling affects *Trex1* KO tumor growth (Supplementary Fig. S10A). *Irf3* deletion reduced IFNβ production to undetectable levels, even in *Trex1*/*Irf3* double KO cells

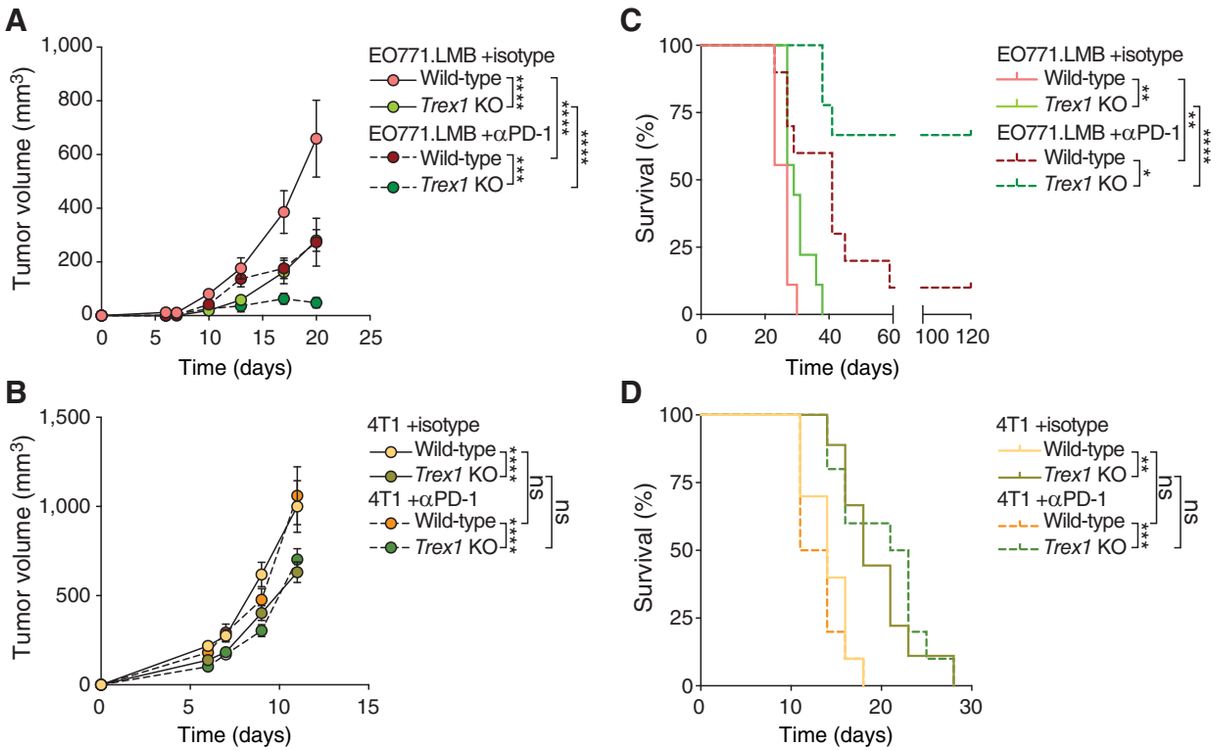

Figure 6.

TREX1 induction reduces immunotherapy efficacy. Growth curves of indicated orthotopically transplanted EO771.LMB (**A**) and 4T1 (**B**) tumors upon treatment with anti-PD-1 or corresponding isotype control; datapoints, mean ± SEM, $n = 9$–10 animals per group. Two-sided *t* test was used to determine statistical significance at the last timepoint; ****, $P < 0.0001$; ***, $P < 0.001$; ns, not significant. Survival of C57BL/6J or BALB/c animals after orthotopic transplantation with indicated EO771.LMB (**C**) or 4T1 (**D**) tumor cells following treatment with anti-PD-1 or corresponding isotype control; $n = 9$–10 animals per group. log-rank test was used to determine statistical significance; ****, $P < 0.0001$; ***, $P < 0.001$; **, $P < 0.01$; *, $P < 0.05$; ns, not significant.

(**Fig. 7B**). TREX1 mRNA, protein levels, and exonuclease activity were significantly decreased in *Irf3* KO cells, indicating that IRF3 plays an essential role in driving *Trex1* gene induction downstream of cGAS-STING (**Fig. 7C** and **D**; Supplementary Fig. S10B).

To assess the impact of IRF3 activation *in vivo*, we transplanted wild-type, *Trex1* KO, *Irf3* KO, and *Trex1*/*Irf3* double KO EO771.LMB tumors into the mammary fat pad of C57BL/6J mice. Consistent with the minimal IFN response observed at baseline (**Fig. 7B**), *Irf3* deletion did not elicit major impacts on EO771.LMB tumor growth or host survival (**Fig. 7E** and **F**). In contrast, *Irf3* deletion rapidly accelerated the growth of EO771.LMB *Trex1* KO cells to rates comparable with wild-type EO771.LMB (777 ± 485 SD mm^3 in *Irf3*/*Trex1* KO tumors vs. 802 ± 430 SD mm^3 in wild-type tumors and 316 ± 315 SD mm^3 in *Trex1* KO tumors at 21 days posttransplantation; **Fig. 7E**; Supplementary Fig. S10C). Animals transplanted with *Irf3*/*Trex1* double KO tumors exhibited a significant decrease in survival relative to animals transplanted with *Trex1* KO tumors (**Fig. 7F**). Differences in tumor growth and overall survival could not be explained by alterations in proliferation of tumor cell lines (Supplementary Fig. S10D). Therefore, TREX1 induction restrains tumor growth by dampening the IRF3-dependent transcriptional response that lies downstream of cGAS-STING activation.

To test whether host sensing of cancer cell–derived IFN signaling is required for the antitumor immune effect seen upon loss of *Trex1* in EO771.LMB cells, we orthotopically transplanted wild-type and *Trex1* KO cells into wild-type and *Ifnar1* KO C57BL/6J host mice, which are deficient for the type I IFN receptor (**Fig. 7G**). The reductions in tumor growth and lifespan extension seen upon *Trex1* deletion were eliminated upon transplantation in *Ifnar1* KO hosts (123 ± 101 SD mm^3 in *Trex1* KO EO771.LMB tumors transplanted to wild-type C57BL/6J animals vs. 787 ± 345 SD mm^3 in *Trex1* KO EO771.LMB tumors transplanted to *Ifnar1* KO C57BL/6J animals at 16 days posttransplantation; **Fig. 7G** and **H**; Supplementary Fig. S10E). Similarly, IFN signaling blockade by treatment with anti-IFNAR-1, significantly accelerated the growth of *Trex1* KO CT26 tumors and reduced survival of their animal hosts (25 ± 30 SD mm^3 in isotype-treated *Trex1* KO CT26 tumors vs. 1,326 ± 921 SD mm^3 in anti-IFNAR-1–treated *Trex1* KO CT26 tumors at 18 days posttransplantation; **Fig. 7I** and **J**; Supplementary Fig. S10F). Taken together, these data indicate that tumor-to-host IFN signaling downstream of intratumoral cGAS-STING activation is necessary to drive tumor regression and extend survival upon *Trex1* deletion.

Discussion

Our work defines intratumoral TREX1 induction as an adaptive, negative feedback mechanism that chromosomally unstable cancer cells employ to dampen cGAS-STING activation, IFN production, and ultimately antitumor immunity. CIN is a hallmark of cancer estimated to occur in 60%–80% of tumors (1). Chromosome mis-segregations that occur during CIN risk inducing cGAS-STING-dependent inflammation and associated immune responses through the generation of cytosolic DNA in the form of micronuclei (3, 5, 6). TREX1 induction

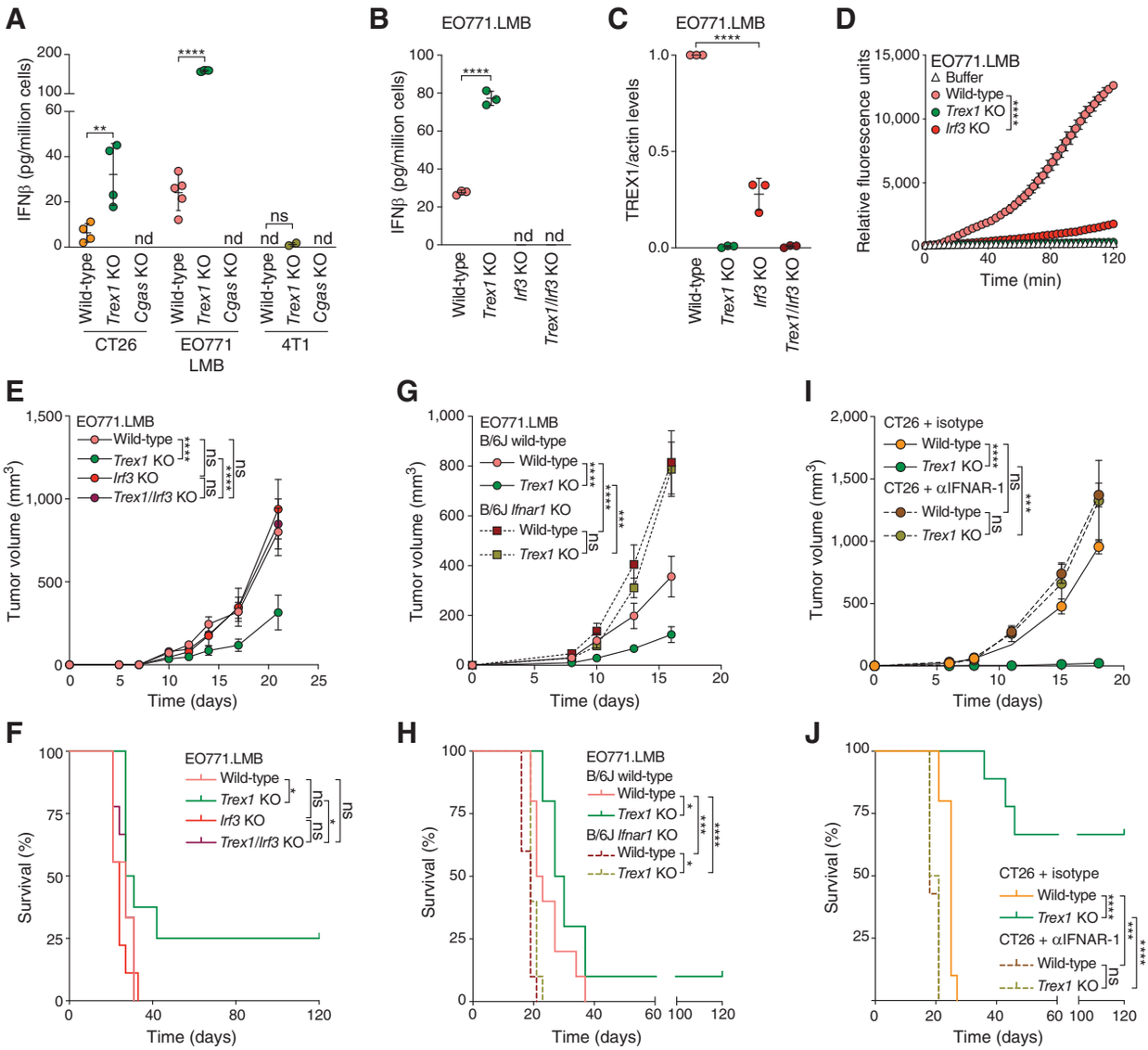

Figure 7.

TREX1 induction promotes tumor growth by suppressing type I IFN. **A** and **B,** ELISA analysis of IFNβ secretion in the indicated cells; mean ± SD, $n = 3$–5 biological replicates; nd, not detected. One-way ANOVA was used to determine statistical significance; ****, $P < 0.0001$; **, $P < 0.01$; ns, not significant. **C,** Quantification of TREX1 relative to corresponding β-actin signal in the indicated EO771.LMB cells; mean ± SD, $n = 3$ experiments. One-way ANOVA was used to determine statistical significance; ****, $P < 0.0001$. **D,** Time course of TREX1 exonuclease activity on dsDNA substrate in indicated EO771.LMB cells; mean ± SD, representative example from $n = 3$ experiments. One-way ANOVA was used to determine statistical significance; ****, $P < 0.0001$. **E,** Growth curves of indicated orthotopically transplanted EO771.LMB tumors; datapoints, mean ± SEM, $n = 9$ animals per group. **F,** Survival of C57BL/6J animals after orthotopic transplantation with indicated EO771.LMB tumor cells; $n = 9$ animals per group. **G,** Growth curves of indicated orthotopically transplanted EO771.LMB tumors into the mammary fat pad of C57BL/6J wild-type or *Ifnar1* KO mice; datapoints, mean ± SEM, $n = 10$ animals per group. **H,** Survival of C57BL/6J wild-type or *Ifnar1* KO animals after orthotopic transplantation with indicated EO771.LMB tumor cells; $n = 10$ animals per group. **I,** Growth curves of indicated injected CT26 tumors upon treatment with anti-IFNAR1 or corresponding isotype control; datapoints, mean ± SEM, $n = 7$–10 animals per group. **J,** Survival of BALB/c animals after injection with indicated CT26 tumor cells upon treatment with anti-IFNAR1 or corresponding isotype control; $n = 7$–10 animals per group. Two-sided *t* test was used to determine statistical significance at the last timepoint in **E**, **G**, and **I**; ****, $P < 0.0001$; ***, $P < 0.001$; ns, not significant. log-rank test was used to determine statistical significance in **F**, **H**, and **J**; ****, $P < 0.0001$; ***, $P < 0.001$; *, $P < 0.05$; ns, not significant.

downstream of cGAS-STING activation enables chromosomally unstable cancers to benefit from increased genomic heterogeneity while ensuring that chromosome mis-segregations are less likely to trigger a strong antitumor immune response. Our results predict that TREX1 inhibition will therefore be an effective strategy to unmask chromosomally unstable cancers from host immunity.

Prior studies have demonstrated that genotoxic treatments, such as high doses of radiotherapy, can increase TREX1 levels in cancer cells through an incompletely understood mechanism (43, 52–54). Although TREX1 has previously been characterized as an ISG, mechanisms of endogenous regulation have not been precisely characterized. Our data indicate that micronuclei induce *Trex1* expression by promoting cGAS-

STING signaling, independently of any exogenous treatment. The resulting increases in TREX1 protein led to corresponding increases in exonuclease activity that likely dampen cGAS activation via enhanced processing of micronuclear DNA (8). Indeed, we showed that *Trex1* deletion significantly increased cGAMP production in chromosomally unstable CT26, EO771.LMB, and 4T1 cells. This effect was further enhanced after elevating micronucleation rates by paclitaxel treatment. TREX1 upregulation may therefore be a common mechanism to suppress cGAS activation by enhancing the metabolism of cytosolic DNA arising from CIN or genotoxic therapies (55). This notion is further supported by earlier observations indicating that *TREX1* expression levels correlate with adverse outcomes across multiple cancer types (56–58).

Limited cGAS activation through TREX1 upregulation has significant impacts on the growth and immune detection of chromosomally unstable cancer cells. We found that intratumoral *Trex1* deletion significantly impeded tumor growth in a manner that depended on intratumoral cGAS-STING, tumor-to-host IFN signaling, and host adaptive immunity. Consistent with these results, we found that intratumoral *Trex1* deletion enhanced the efficacy of anti-PD-1 immune checkpoint blockade therapy. The observed increases in cGAMP and IFNβ production in paclitaxel-treated *Trex1* KO cells suggest that TREX1-focused therapies may work well in combination with genotoxic or antimitotic treatments that increase cytosolic DNA levels. Further work will be necessary to test this possibility.

Prior work demonstrated that targeting TREX1 exonuclease activity within the host immune compartment could slow the growth of H31m1, a syngeneic, chemically induced sarcoma model (59). In this setting, inhibition of TREX1 exonuclease activity within the host compartment is thought to enhance antitumor immunity by stabilizing tumor-derived DNA that may be incorporated into tumor infiltrating immune cells. A key distinction in our data is the finding that the increased levels of TREX1 and cytosolic DNA within the tumor compartment may offer an improved window for therapeutic strategies based on TREX1 inhibition. Ultimately, targeting TREX1 within both the tumor and host compartments is likely to offer the most potent impacts on tumor growth and antitumor immunity.

Our data indicate that intratumoral *Trex1* deletion has a major impact on the growth and immune response against the CT26 and EO771.LMB models, compared with a much weaker, cGAS-independent effect on growth in the 4T1 model. Differences in CIN and cGAS regulation are unlikely to account for these contrasting effects. CT26, EO771.LMB, and 4T1 models all maintained cGAS-STING expression, possessed similar amounts of micronuclei, and exhibited increased cGAMP production upon *Trex1* deletion. Despite these similarities, 4T1 cells were unable to activate IFNβ expression downstream of cGAS-STING—even upon stimulation with HT-DNA—suggesting that additional factors prevent IFN response even after maximal STING stimulation (14). The contrast between these models supports the notion that host sensing of tumor-derived IFNβ is a critical mediator of antitumor immunity in *Trex1* KO tumors. Indeed, wild-type and *Trex1* KO EO771.LMB tumors exhibited comparable growth upon transplantation into *Ifnar1* KO mice, and treatment with anti-IFNAR-1 antibodies accelerated the growth of *Trex1* KO CT26 tumors. These observations indicate that TREX1 upregulation shields chromosomally unstable tumors from host adaptive immunity by limiting intratumoral type I IFN signaling and suggest that an intact, intratumoral cGAS-STING-IFN response may be critical for the selection of patients most likely to benefit from therapeutic STING agonism or TREX1 inhibition.

STING agonism has emerged as a key strategy to potentiate antitumor immune responses; however, clinical gains have been limited thus far (48, 60). The precise causes of limited clinical efficacy are poorly understood but may be related to dose limiting toxicities or counterproductive effects within some immune compartments (61, 62). The data presented here suggest that TREX1 inhibition may present an alternative path to STING agonism that offers a more targeted therapeutic opportunity rooted in the observed increases in intratumoral TREX1 expression. The abundance of cytoplasmic DNA within tumor cells is further expected to cause TREX1 inhibition to offer an improved therapeutic window relative to STING agonists. Indeed, we have previously observed that *TREX1* deletion has minimal impacts upon cGAMP production or ISG expression in non-tumorigenic, chromosomally stable cells that lack cytosolic DNA (8). Therefore, inhibition of TREX1 nuclease activity may provide a unique therapeutic opportunity to direct host immune responses against chromosomally unstable cancer cells while sparing non-tumorigenic cells that typically lack high levels of cytosolic DNA. Finally, our data also suggest that assessing the intrinsic capacity of tumor cells to generate a type I IFN response downstream of cGAS-STING will be a critical predictor of the success of TREX1 inhibitors, highlighting biomarker-based strategies that can guide the placement of these therapeutics in the clinic.

Authors' Disclosures

S.F. Bakhoum reports personal fees from Volastra Therapeutics and Meliora Therapeutics outside the submitted work; in addition, S.F. Bakhoum has a patent for Targeting CIN and cGAS-STING in cancer pending and issued. J. Maciejowski reports a patent for targeting cGAS-STING pathway in cancer pending. No disclosures were reported by the other authors.

Authors' Contributions

E. Toufektchan: Conceptualization, resources, data curation, formal analysis, supervision, funding acquisition, investigation, visualization, methodology, writing–original draft, writing–review and editing. **A. Dananberg:** Data curation, formal analysis, investigation, writing–review and editing. **J. Striepen:** Data curation, formal analysis, investigation, writing–review and editing. **J.H. Hickling:** Data curation, formal analysis, investigation. **A. Shim:** Data curation, formal analysis, investigation, writing–review and editing. **Y. Chen:** Data curation, formal analysis, investigation, writing–review and editing. **A. Nichols:** Data curation, investigation. **M.A. Duran Paez:** Investigation, methodology. **L. Mohr:** Data curation, investigation. **S.F. Bakhoum:** Conceptualization, resources, supervision, funding acquisition, writing–review and editing. **J. Maciejowski:** Conceptualization, resources, data curation, formal analysis, supervision, funding acquisition, investigation, writing–original draft, writing–review and editing.

Acknowledgments

Work in J. Maciejowski's laboratory is supported by the NCI (R00CA212290; R37CA261183; R01CA270102; P30CA008748), the Pew Charitable Trusts, the V Foundation, the Starr Cancer Consortium, the Pershing Square Sohn Cancer Research Alliance, the Frank A. Howard Scholars Program, the Mary Kay Ash Foundation, and the Geoffrey Beene, Ludwig, and Experimental Therapeutics Centers at MSKCC. Work in the Bakhoum lab is partly supported by NIH/NCI: P50CA247749, DP5OD026395, R01CA256188, R01CA280572, P30-CA008748; Congressionally Directed Medical Research Program BC201053 and the Era of Hope Award; Burroughs Wellcome Fund (BWF); Josie Robertson Foundation; the Mark Foundation for Cancer Research, Mary Kay Ash Foundation, the STARR Cancer Consortium, and the Cycle for Survival Fund. E. Toufektchan received support from the Francois Wallace Monahan and the Philippe Foundation.

We thank members of the Maciejowski lab for critical reading of this manuscript, A. Liberchuk for technical assistance, and C. Krumm for help with the 3′→5′ exonuclease activity assay.

Note

Supplementary data for this article are available at Cancer Immunology Research Online (http://cancerimmunolres.aacrjournals.org/).

Received December 22, 2023; revised February 6, 2024; accepted February 23, 2024; published first February 26, 2024.

References

1. Cimini D. Merotelic kinetochore orientation, aneuploidy, and cancer. Biochim Biophys Acta 2008;1786:32–40.
2. Bakhoum SF, Cantley LC. The multifaceted role of chromosomal instability in cancer and its microenvironment. Cell 2018;174:1347–60.
3. Hatch EM, Fischer AH, Deerinck TJ, Hetzer MW. Catastrophic nuclear envelope collapse in cancer cell micronuclei. Cell 2013;154:47–60.
4. Liu S, Kwon M, Mannino M, Yang N, Renda F, Khodjakov A, et al. Nuclear envelope assembly defects link mitotic errors to chromothripsis. Nature 2018; 561:551–5.
5. Harding SM, Benci JL, Irianto J, Discher DE, Minn AJ, Greenberg RA. Mitotic progression following DNA damage enables pattern recognition within micronuclei. Nature 2017;548:466–70.
6. Mackenzie KJ, Carroll P, Martin C-A, Murina O, Fluteau A, Simpson DJ, et al. cGAS surveillance of micronuclei links genome instability to innate immunity. Nature 2017;548:461–5.
7. Sun L, Wu J, Du F, Chen X, Chen ZJ. Cyclic GMP-AMP synthase is a cytosolic DNA sensor that activates the type I interferon pathway. Science 2013;339: 786–91.
8. Mohr L, Toufektchan E, von Morgen P, Chu K, Kapoor A, Maciejowski J. ER-directed TREX1 limits cGAS activation at micronuclei. Mol Cell 2021;81:724–38.
9. MacDonald KM, Nicholson-Puthenveedu S, Tageldein MM, Khasnis S, Arrowsmith CH, Harding SM. Antecedent chromatin organization determines cGAS recruitment to ruptured micronuclei. Nat Commun 2023;14:556.
10. Ablasser A, Goldeck M, Cavlar T, Deimling T, Witte G, Röhl I, et al. cGAS produces a 2'-5'-linked cyclic dinucleotide second messenger that activates STING. Nature 2013;498:380–4.
11. Diner EJ, Burdette DL, Wilson SC, Monroe KM, Kellenberger CA, Hyodo M, et al. The innate immune DNA sensor cGAS produces a noncanonical cyclic dinucleotide that activates human STING. Cell Rep 2013;3:1355–61.
12. Gao P, Ascano M, Zillinger T, Wang W, Dai P, Serganov AA, et al. Structure-function analysis of STING activation by c [G (2′, 5′) pA (3′, 5′) p] and targeting by antiviral DMXAA. Cell 2013;154:748–62.
13. Wu J, Sun L, Chen X, Du F, Shi H, Chen C, et al. Cyclic GMP-AMP is an endogenous second messenger in innate immune signaling by cytosolic DNA. Science 2013;339:826–30.
14. Ablasser A, Chen ZJ. cGAS in action: expanding roles in immunity and inflammation. Science 2019;363:eaat8657.
15. Ishikawa H, Ma Z, Barber GN. STING regulates intracellular DNA-mediated, type I interferon-dependent innate immunity. Nature 2009;461:788–92.
16. Ishikawa H, Barber GN. STING is an endoplasmic reticulum adaptor that facilitates innate immune signalling. Nature 2008;455:674–8.
17. Liu S, Cai X, Wu J, Cong Q, Chen X, Li T, et al. Phosphorylation of innate immune adaptor proteins MAVS, STING, and TRIF induces IRF3 activation. Science 2015;347:aaa2630.
18. Wang H, Hu S, Chen X, Shi H, Chen C, Sun L, et al. cGAS is essential for the antitumor effect of immune checkpoint blockade. Proc Natl Acad Sci U S A 2017; 114:1637–42.
19. Hu J, Sánchez-Rivera FJ, Wang Z, Johnson GN, Ho Y-J, Ganesh K, et al. STING inhibits the reactivation of dormant metastasis in lung adenocarcinoma. Nature 2023;616:806–13.
20. Li T, Chen ZJ. The cGAS-cGAMP-STING pathway connects DNA damage to inflammation, senescence, and cancer. J Exp Med 2018;215:1287–99.
21. Barber GN. STING: infection, inflammation and cancer. Nat Rev Immunol 2015; 15:760–70.
22. Konno H, Yamauchi S, Berglund A, Putney RM, Mulé JJ, Barber GN. Suppression of STING signaling through epigenetic silencing and missense mutation impedes DNA damage mediated cytokine production. Oncogene 2018; 37:2037–51.
23. Bakhoum SF, Ngo B, Laughney AM, Cavallo J-A, Murphy CJ, Ly P, et al. Chromosomal instability drives metastasis through a cytosolic DNA response. Nature 2018;553:467–72.
24. Li J, Hubisz MJ, Earlie EM, Duran MA, Hong C, Varela AA, et al. Non-cell-autonomous cancer progression from chromosomal instability. Nature 2023; 620:1080–8.
25. Carozza JA, Böhnert V, Nguyen KC, Skariah G, Shaw KE, Brown JA, et al. Extracellular cGAMP is a cancer-cell-produced immunotransmitter involved in radiation-induced anticancer immunity. Nature Cancer 2020;1:184–96.
26. Li J, Duran MA, Dhanota N, Chatila WK, Bettigole SE, Kwon J, et al. Metastasis and immune evasion from extracellular cGAMP hydrolysis. Cancer Discov 2021; 11:1212–27.
27. Stetson DB, Ko JS, Heidmann T, Medzhitov R. Trex1 prevents cell-intrinsic initiation of autoimmunity. Cell 2008;134:587–98.
28. Mazur DJ, Perrino FW. Excision of 3′ Termini by the Trex1 and TREX2 3′→ 5′ Exonucleases characterization of the recombinant proteins. J Biol Chem 2001; 276:17022–9.
29. Perrino FW, Miller H, Ealey KA. Identification of a 3'→5'-exonuclease that removes cytosine arabinoside monophosphate from 3' termini of DNA. J Biol Chem 1994;269:16357–63.
30. Mazur DJ, Perrino FW. Identification and expression of the TREX1 and TREX2 cDNA sequences encoding mammalian 3'→5' exonucleases. J Biol Chem 1999; 274:19655–60.
31. Yang Y-G, Lindahl T, Barnes DE. Trex1 exonuclease degrades ssDNA to prevent chronic checkpoint activation and autoimmune disease. Cell 2007;131:873–86.
32. Crow YJ, Manel N. Aicardi–Goutières syndrome and the type I interferonopathies. Nat Rev Immunol 2015;15:429–40.
33. Rice GI, Rodero MP, Crow YJ. Human disease phenotypes associated with mutations in TREX1. J Clin Immunol 2015;35:235–43.
34. Morita M, Stamp G, Robins P, Dulic A, Rosewell I, Hrivnak G, et al. Gene-targeted mice lacking the Trex1 (DNase III) 3'→5' DNA exonuclease develop inflammatory myocarditis. Mol Cell Biol 2004;24:6719–27.
35. Grieves JL, Fye JM, Harvey S, Grayson JM, Hollis T, Perrino FW. Exonuclease TREX1 degrades double-stranded DNA to prevent spontaneous lupus-like inflammatory disease. Proc Natl Acad Sci U S A 2015;112:5117–22.
36. Xiao N, Wei J, Xu S, Du H, Huang M, Zhang S, et al. cGAS activation causes lupus-like autoimmune disorders in a TREX1 mutant mouse model. J Autoimmun 2019;100:84–94.
37. Rego SL, Harvey S, Simpson SR, Hemphill WO, McIver ZA, Grayson JM, et al. TREX1 D18N mice fail to process erythroblast DNA resulting in inflammation and dysfunctional erythropoiesis. Autoimmunity 2018;51:333–44.
38. Simpson SR, Rego SL, Harvey SE, Liu M, Hemphill WO, Venkatadri R, et al. T Cells produce IFN-α in the TREX1 D18N model of Lupus-like autoimmunity. J Immunol 2020;204:348–59.
39. Gray EE, Treuting PM, Woodward JJ, Stetson DB. Cutting Edge: cGAS is required for lethal autoimmune disease in the Trex1-deficient mouse model of aicardi–goutières syndrome. J Immunol 2015;195:1939–43.
40. Ablasser A, Hemmerling I, Schmid-Burgk JL, Behrendt R, Roers A, Hornung V. TREX1 deficiency triggers cell-autonomous immunity in a cGAS-dependent manner. J Immunol 2014;192:5993–7.
41. Rodriguez de la Fuente L, Law AMK, Gallego-Ortega D, Valdes-Mora F. Tumor dissociation of highly viable cell suspensions for single-cell omic analyses in mouse models of breast cancer. STAR Protoc 2021;2:100841.
42. Marcus A, Mao AJ, Lensink-Vasan M, Wang L, Vance RE, Raulet DH. Tumor-derived cGAMP Triggers a STING-mediated interferon response in non-tumor cells to activate the NK cell response. Immunity 2018;49:754–63.
43. Vanpouille-Box C, Alard A, Aryankalayil MJ, Sarfraz Y, Diamond JM, Schneider RJ, et al. DNA exonuclease Trex1 regulates radiotherapy-induced tumour immunogenicity. Nat Commun 2017;8:15618.
44. Pereira-Lopes S, Celhar T, Sans-Fons G, Serra M, Fairhurst A-M, Lloberas J, et al. The exonuclease Trex1 restrains macrophage proinflammatory activation. J Immunol 2013;191:6128–35.
45. Xu J, Zoltick PW, Gamero AM, Gallucci S. TLR ligands up-regulate Trex1 expression in murine conventional dendritic cells through type I Interferon and NF-κB-dependent signaling pathways. J Leukoc Biol 2014;96:93–103.
46. Maltbaek JH, Cambier S, Snyder JM, Stetson DB. ABCC1 transporter exports the immunostimulatory cyclic dinucleotide cGAMP. Immunity 2022;55:1799–812.
47. Liu H, Zhang H, Wu X, Ma D, Wu J, Wang L, et al. Nuclear cGAS suppresses DNA repair and promotes tumorigenesis. Nature 2018;563:131–6.
48. Samson N, Ablasser A. The cGAS–STING pathway and cancer. Nature Cancer 2022;3:1452–63.
49. Corrales L, Glickman LH, McWhirter SM, Kanne DB, Sivick KE, Katibah GE, et al. Direct activation of STING in the tumor microenvironment leads to potent and systemic tumor regression and immunity. Cell Rep 2015;11:1018–30.
50. Gros A, Robbins PF, Yao X, Li YF, Turcotte S, Tran E, et al. PD-1 identifies the patient-specific CD8+ tumor-reactive repertoire infiltrating human tumors. J Clin Invest 2014;124:2246–59.
51. Wu J, Dobbs N, Yang K, Yan N. Interferon-independent activities of mammalian STING mediate antiviral response and tumor immune evasion. Immunity 2020; 53:115–26.
52. Tomicic MT, Aasland D, Nikolova T, Kaina B, Christmann M. Human three prime exonuclease TREX1 is induced by genotoxic stress and involved in

protection of glioma and melanoma cells to anticancer drugs. Biochim Biophys Acta 2013;1833:1832–43.
53. Vanpouille-Box C, Formenti SC, Demaria S. TREX1 dictates the immune fate of irradiated cancer cells. Oncoimmunology 2017;6:e1339857.
54. Christmann M, Tomicic MT, Aasland D, Berdelle N, Kaina B. Three prime exonuclease I (TREX1) is Fos/AP-1 regulated by genotoxic stress and protects against ultraviolet light and benzo(a)pyrene-induced DNA damage. Nucleic Acids Res 2010;38:6418–32.
55. Wang C-J, Lam W, Bussom S, Chang H-M, Cheng Y-C. TREX1 acts in degrading damaged DNA from drug-treated tumor cells. DNA Repair 2009;8:1179–89.
56. Dong X, Jiao L, Li Y, Evans DB, Wang H, Hess KR, et al. Significant associations of mismatch repair gene polymorphisms with clinical outcome of pancreatic cancer. J Clin Oncol 2009;27:1592–9.
57. Zhu H, Li X, Zhang X, Chen D, Li D, Ren J, et al. Polymorphisms in mismatch repair genes are associated with risk and microsatellite instability of gastric cancer, and interact with life exposures. Gene 2016;579:52–7.
58. Prati B, da Silva Abjaude W, Termini L, Morale M, Herbster S, Longatto-Filho A, et al. Three prime repair exonuclease 1 (TREX1) expression correlates with cervical cancer cells growth *in vitro* and disease progression *in vivo*. Sci Rep 2019;9:351.
59. Hemphill WO, Simpson SR, Liu M, Salsbury Jr FR, Hollis T, Grayson JM, et al. TREX1 as a novel immunotherapeutic target. Front Immunol 2021;12:660184.
60. Demaria O, De Gassart A, Coso S, Gestermann N, Di Domizio J, Flatz L, et al. STING activation of tumor endothelial cells initiates spontaneous and therapeutic antitumor immunity. Proc Natl Acad Sci U S A 2015;112:15408–13.
61. Li S, Mirlekar B, Johnson BM, Brickey WJ, Wrobel JA, Yang N, et al. STING-induced regulatory B cells compromise NK function in cancer immunity. Nature 2022;610:373–80.
62. Kuhl N, Linder A, Philipp N, Nixdorf D, Fischer H, Veth S, et al. STING agonism turns human T cells into interferon-producing cells but impedes their functionality. EMBO Rep 2023;24:e55536.